

On the Break-up of a Turbulent Liquid Wall Sheet

T.C. Fu¹, P.M. Bardet², E.E. Hackett¹ and A. Kowalski¹

¹Hydromechanics Department
Naval Surface Warfare Center, Carderock Division, Bethesda, MD, USA

²Department of Mechanical and Aerospace Engineering
The George Washington University, Washington, D.C., USA

Abstract

A wide range of applications involve the break-up of liquid jets into spray. This break-up of a turbulent liquid wall jet is a complex multiphase flow problem. While circular liquid jets have been studied extensively, geometrical and scale differences make the break-up of a liquid wall sheet different from both circular free and wall jets, although the sheet break-up mechanisms can be similar. Currently, direct simulation of these processes is impractical due to the large range of scales involved and the requirements on grid resolution and computation time. Because of these limitations, semi-empirical closure models are necessary. This paper describes results from a set of experiments focused on the break-up of a turbulent liquid wall sheet. The focus of the effort was to investigate physical mechanisms and provide data for assessment of numerical simulations of the bulk properties of the sheet and spray.

Introduction

Experimental research on liquid sheet break-up is performed in order to improve our understanding of the break-up mechanisms. A wide range of applications involve the break-up of liquid jets. Circular liquid jets have been studied extensively, e.g. [5]. Geometrical and scale differences make the break-up of a liquid wall sheet different from both circular free and wall jets, although the physical mechanisms leading to the sheet's break-up can be similar [1]. The physics of a liquid wall sheet break-up are generally described as resulting from advection and diffusion of vortices within the turbulent boundary layer to the liquid surface [2, 9]. These structures cause the liquid surface to roughen, and subsequently create ligaments, which ultimately results in spray production. As examined by Sarpkaya and Merrill [8], ligaments elongate until surface tension effects result in the tip pinching off of a ligament to create a droplet. Although, there is agreement on the qualitative aspects of this process, an understanding thorough enough to implement robust semi-empirical models of it is lacking.

In this study, we perform experiments examining the break-up of a turbulent wall-bounded sheet. Shadowgraphy on an inclined wall-bounded liquid sheet was performed using backlighting and a high-speed camera. The experiment involved pumping water along the underside of a plate inclined relative to horizontal. Downstream of the nozzle, the sheet began to break-up into spray and eventually separated from the plate. These experiments were purposely focused on relatively large-scales (sheet width ~0.3 m).

Experiment

For the study, an inclined liquid wall sheet was generated and imaged with a number of high-speed cameras. These images were analyzed using custom image processing algorithms for detecting and characterizing droplets, their trajectories, the air-water interface, and air entrainment.

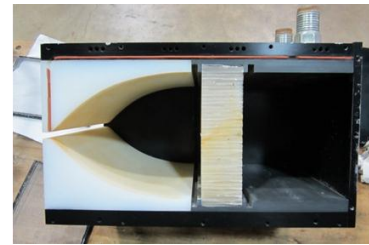


Figure 1. Image of the nozzle and internal flow straighteners. Note the two screens have been removed.

Experimental Setup

The test apparatus consisted of a nozzle, flat plate, and frame to hold both the nozzle and flat plate at an angle relative to horizontal. The experiments were performed in the 140-ft. Basin at the Naval Surface Warfare Center, Carderock Division. The basin was drained to approximately 0.5 m and water was pumped using a 0.02 m³/s (300 gpm) centrifugal pump to the nozzle. Inside the nozzle, there were two screens and a honeycomb for flow straightening (see Figure 1), and the flow had a non-zero initial turbulence level at the nozzle exit. The sheet surface was slightly roughened at the nozzle exit; however, no ligaments or droplets were observed there. Specifically, no droplets were observed within the first 6 cm of the nozzle outlet. Thus, at the nozzle, the onset of surface roughness was observed, but the onset of primary break-up occurred after the nozzle exit. These nozzle exit conditions are important because it has been shown that the onset of jet breakup is dependent on the turbulence conditions at the jet exit, e.g. [6]. Direct measurement of these initial turbulence levels were not able to be made. In addition, based on previous research [4], it was assumed that any aerodynamic effects on the flow were negligible. The tests were performed in ambient air at normal temperature and pressure.

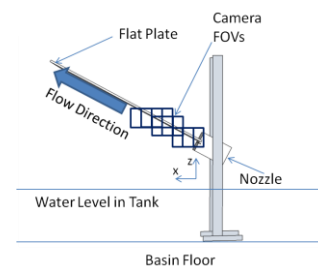


Figure 2. Schematic of the experimental apparatus for generating an inclined liquid wall sheet.

Nominal flow velocities at the nozzle exit of 7, 8, and 8.6 m/s were examined. The nozzle aperture was 30.5 cm × 0.635 cm. Both the nozzle and plate were set at a 31° angle relative to horizontal, and the flow occurred on the underside of the plate. Due to the flow speeds and size of the nozzle aperture, multiple camera fields-of-view (FOV) were required to image the sheet

through the point at which it separated from the plate. Figure 2 shows a schematic of the frame and nozzle setup along with approximate positions of the various camera FOVs.

A 1024×1024 pixel² Photronics SA1 CMOS camera with a dynamic range of 12 bits and a 70 mm lens was used. The f-stop was set to 2.8 to make the depth-of-field as small as possible in an effort to isolate a cross section at the centerline of the sheet. The image magnification was approximately 35×35 cm² (see Figure 3). Using ~50% overlap between consecutive FOVs, seven different positions along the sheet were imaged for the highest flow speed. Backlighting was provided by two ARRI 600 Watt lights, which were overlapped and diffused to provide the required illumination. Images were acquired at 500 fps with shutter speeds between 58-66 μ s. Five thousand images were acquired at each camera position.

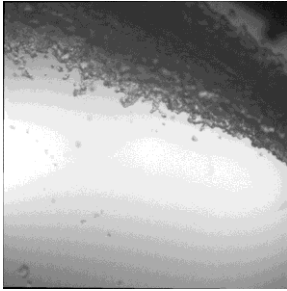


Figure 3. Sample image of an inclined liquid wall sheet (35 cm \times 35 cm). The right side of the image is ~16 cm downstream of the nozzle outlet

Image Processing

Acquired images were analyzed to characterize the air-water interface. In addition, the location at which the sheet separated from the plate was determined. Details of the image processing algorithms are described in [3], but brief descriptions are below:

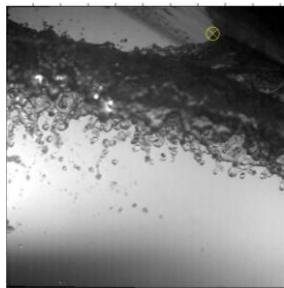


Figure 4. Sample result of the separation length-scale processing. The yellow encircled \times marks the identified separation point for this image.

Separation Length-Scales

Image processing algorithms were used to obtain the location at which the sheet separated from the plate. Because the location of the plate in the images was often obscured by the sheet itself (see Figure 3), calibration images were taken at the focal point of the camera. These images were analyzed using Hough transforms to obtain the line corresponding to the in-focus plate location for each of the camera positions, and a Sobel edge detection routine was applied in a region surrounding the separation of the sheet from the plate. Edges that fell within ± 0.3 mm (± 1 pixel) of the plate were identified. Figure 4 shows a sample result obtained from this process.

Air-Water Interface

A rigorous image processing approach for identifying the air-water interface was implemented in order to retain as much of the detail in the surface roughness characteristics as possible. First, to determine an approximate location of the interface a Canny edge

detection routine was applied, and a linear fit to the detected edges was computed. A Sobel edge detection routine was then applied, and the air-water interface edge contour was defined as the edge with the strongest gradient. Additional processing as described in [3] resulted in a selection of contour points that were positioned along the air-water interface of the spray sheet. A sample result from this algorithm is shown in Figure 5.

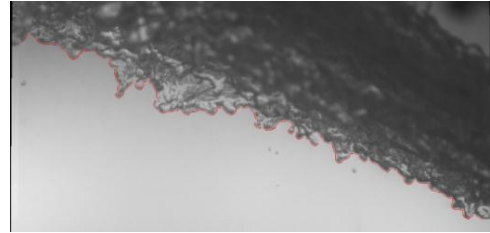


Figure 5. Example of the detected air-water interface. The red line shows the detected air-water interface.

Surface Tracking

The flow meter provided an estimate of the sheet velocity based on mass flow conservation, and these values (7 m/s, 8 m/s, and 8.6 m/s) are used throughout this paper for referring to specific datasets. However, the flow meter is only accurate to approximately 2% of the flow rate, and the repeatability of the flow rate was only accurate to approximately $\pm 2.5 \times 10^{-4}$ m³/s (± 4 gpm). The estimated velocity based on mass flow conservation provides an average value over the sheet thickness rather than at a specific location. In order to account for some of these inaccuracies and to obtain a more reliable estimate of the surface sheet velocity, cross-correlations were performed to estimate sheet speed at the free-surface.

A sample result for the 8.6 m/s flow case of this analysis is shown in Figure 6. The two lines show the air-water interfaces for the image-pair including a 2 pixel expansion of the interface. The vectors denote the interface displacement in pixels between the two frames, which of course can easily be converted to a velocity using the frame rate (500 fps) and image magnification. The computed velocities were used to examine the sheet surface speed as a function of distance from the nozzle.

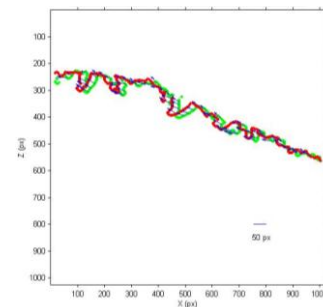


Figure 6. Example of the correlation of the air-water interface between two consecutive frames for the 8.6 m/s flow speed. The two lines show the interfaces for each of the images, and the vectors denote the interface displacement in pixels between the two frames. A scale vector is also provided in the figure.

Results

The coordinate system for presentation of the experimental results has an arbitrary origin located at the bottom right corner of the FOV closest to the nozzle. All results presented are referenced to this origin. The center of the nozzle outlet relative to this origin is $x = -0.87$ cm and $z = 11.57$ cm (± 0.2 cm). The coordinate system is defined such that the positive x -direction is in the direction of the flow and positive z is opposite the direction of gravity (see Figure 2).

The relevant non-dimensional parameters for this flow are the Reynolds, Froude, and Weber numbers. For sheet speeds from 5-9 m/s, the Reynolds number, $v_s L/\nu$, where v_s is the sheet velocity, L is the relevant length scale, taken here to be the sheet thickness, 0.635 cm, and ν is the kinematic viscosity of fresh water at 20° C, 1.004×10^{-6} m²/s, ranged from 31,624-56,922. The Froude number, v_s^2/gL , where g is acceleration due to gravity, ranged from 402-1,301. The Weber number, $\rho v_s^2 L/\gamma$, where γ and ρ , are the surface tension and density of fresh water at 20° C, respectively, 0.0728 N/m and 998.2 kg/m³, ranged from 2,177-7,053.

Separation Length-Scales

The separation point of the sheet with the plate varied in time and space for all three speeds. Figure 7 shows these variations, where the location of the separation point in the x direction is plotted versus time. Because of the overlapping FOVs, there were two FOVs that clearly captured the separation point for the 8 m/s flow speed, so two results are shown. As the speed increases, the separation point occurs further from the nozzle, as expected. There is clearly good agreement between the results for the two independently analyzed runs for the 8 m/s flow speed. The separation point becomes increasingly more stable as the flow speed increases. For the 8 m/s and the 7 m/s case, there is a significant oscillation on a time-scale of roughly 1 s, whose amplitude decays as the flow speed increases. It is unclear why this behavior occurs, but it may be related to an intrinsic frequency because the 7 m/s speed was near the lower limit of the sheet instability. At 6 m/s, the sheet did not clearly break-up prior to separation from the plate, but was still turbulent (albeit at much lower intensity).

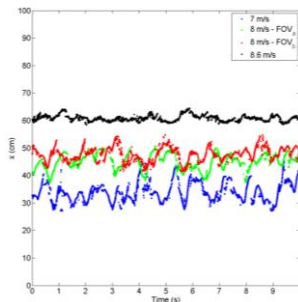


Figure 7. Location in the x direction of the sheet separation from the plate as a function of time for three different flow speeds. Two camera FOVs captured the separation point for the 8 m/s case, so two estimates are shown for that speed.

Sheet Characteristics

Sheet thickness in the z direction versus distance from the nozzle in the x direction was computed using the plate location determined from the calibration images and the extracted air-water interface. The sheet thickness up to the separation point is shown in Figure 8. If one is interested in obtaining the sheet thickness perpendicular to the plate, then values shown in Figure 8 should be divided by $\cos(31^\circ)$ to account for the angle of the plate. For $x < 20$ cm from the nozzle, the sheet thickness for all the speeds is similar. Following this region, for a given distance downstream from the nozzle, the lower the flow speed the thicker the sheet. The sheet reaches its thickest point at separation. Extrapolation of the thickness curves back to the nozzle's position, shown as single points in Figure 8, results in values slightly larger than the nozzle orifice (but within one standard deviation), which is indicated with the green point. Care should be taken in interpreting these thickness results. Because the thickness is computed as the difference between the extracted air-water interface and the plate location, areas of high void fraction can be included in the estimate of the thickness. In addition, the ligaments are also included.

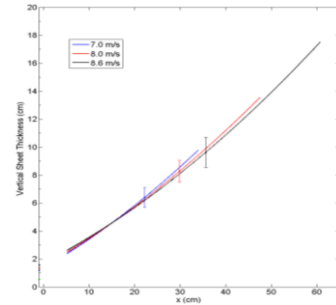


Figure 8. Sheet thickness (in z) versus distance downstream from the nozzle in the x direction up to the separation point for the three flow speeds. Error bars show sample $\pm\sigma$.

The variability of the sheet thickness, represented as the standard deviation of the mean interface, is mostly due to the presence of ligaments along the air-water interface. The standard deviation of the air-water interface can therefore be considered to show a characteristic scale of the ligaments, which increases as the flow speed increases. This increase is partly attributable to the fact that the sheet remains attached to the plate further downstream for the higher flow speeds, which allows the boundary layer to thicken and contain larger turbulent scales. These larger scales manifest in larger ligaments on the sheet surface.

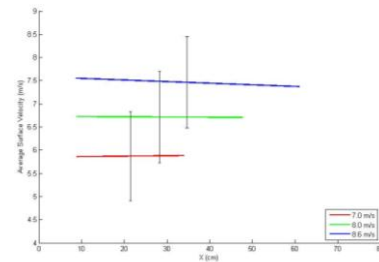


Figure 9. Average surface sheet velocity magnitude versus distance from the nozzle in the x direction up to the separation point. Error bars show sample $\pm\sigma$.

In addition to the sheet thickness, we also examined how the sheet surface speed varies with distance from the nozzle. Figure 9 shows the temporal mean sheet velocity magnitude as a function of distance from the nozzle in the x direction. There is a slight decrease in the surface sheet speed as the sheet thickens. The reduction in speed is the most apparent in the highest flow speed case because the sheet remains attached to the plate further from the nozzle, allowing it to thicken more than for the other two cases. This reduction for the highest flow speed is reasonably consistent with the previous results [2], where the surface speed of an annular wall jet reduced by approximately 10% over a streamwise distance of 100 jet diameters relative to the onset of surface roughness. Here, we find a 5% reduction in speed at 100 sheet thicknesses downstream from the nozzle. The error bars show sample one standard deviation of the velocity time series, which represents the magnitude of instantaneous variations about the mean. In this case, part of this variation stems from the magnitude of the turbulent fluctuations. Thus, one can also view the error bars as representative of the magnitude of turbulent fluctuations. Because each of the temporal mean velocity estimates is based-on 5000 samples, the standard error on the mean value is much smaller than the standard deviation. The standard error is about ± 1 cm/s, or a factor of 70.7 less than the shown standard deviations.

Mean Free-Surface Evolution

For the 8.6 m/s flow rate, images were taken from three angles: from below and two views of the layer through the back transparent plate, one normal to the plate to reveal spatial evolution of the flow, the other is a side view at a 30° angle from

this plane to gain access to surface profile. From these images it could be seen that at the free-surface of the layer, regularly spaced longitudinal waves rapidly form (Figure 7a). These waves stay spatially coherent for long distances, and are likely due to Goertler vortices created in the concave section of the nozzle. This is confirmed by Figure 7b where two downwelling regions are identifiable near the exit; these regions are the signature of a series of pairs of counter-rotating streamwise vortices.

These longitudinal surface waves are highly vortical in nature and rapidly grow in amplitude under the combined actions of layer thickening, viscous diffusion, vortex pairing, vortices induced flow, and gravity. The vortex tubes core increases in diameter due to: (i) vortex stretching (or shrinking) associated with negative streamwise gradients of streamwise velocity; (ii) viscous diffusion; and (iii) vortex pairing, i.e. longitudinal waves merging. Additionally, the longitudinal vortices travel towards the surface under the induced flow they generate. Finally, these gravity-capillary waves (cm-wavelengths) are pulled downward by the gravitational acceleration.

Near the separation point, the wavelength has increased significantly and the layer is made of rolled waves and thin and flat regions between them (Figure 7c). Most of the momentum is carried by the waves; the thin regions are travelling significantly slower than the waves. The two regions will separate at different downstream locations with the large waves separating first. Due to spatial and temporal oscillations associated with the initiation and evolution of the waves, the latter fluctuate in the spanwise direction and entrain different amount of momentum. Hence, the large waves separation point fluctuates both axially and transversally, which in turn strongly affects the thin regions. This mechanism is related to the oscillations mentioned above.

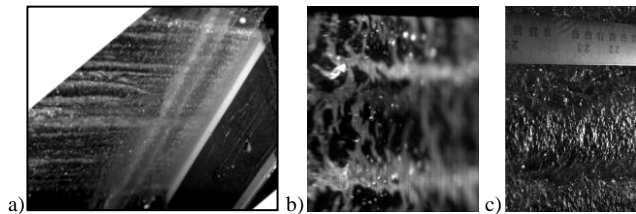


Figure 7. Free surface profiles, flow direction is from right to left, (a) image of the free-surface from below (first 30 cm), the nozzle is on the right of the frame; (b) side view 12 cm from nozzle exit; (c) side view 58 cm from nozzle exit.

Air Entrainment

Several sources of air entrainment have been observed in the layer. For the highest flow rate (8.6 m/s), at the location where the liquid jet connects with the plate, air is injected into the layer along the wall (Figure 8a). There is also evidence of air entrainment on the side of the longitudinal vortices similar to simulations [10], Figure 8b & 8c. Air bubbles are also injected into the fluid by turbulent shear and surface normal vorticity.

Conclusions

The experimental results presented in this paper discuss both the characteristics of the turbulent wall sheet as well as descriptions of associated physical mechanisms. The sheet thickens with distance downstream of the nozzle, as it slows and entrains air, and eventually separates from the plate. This separation distance is further downstream for higher flow speeds, and is more stable. The characteristic scale of the ligaments increases with flow speed and distance from the nozzle. The droplet shape and size distributions do not vary much with flow speed, but the droplet velocity distributions do. Droplet characteristics as a function of distance from the nozzle are also examined as well as their trajectories, where similar to the results for the various flow speeds, the primary variations are in droplet velocities.

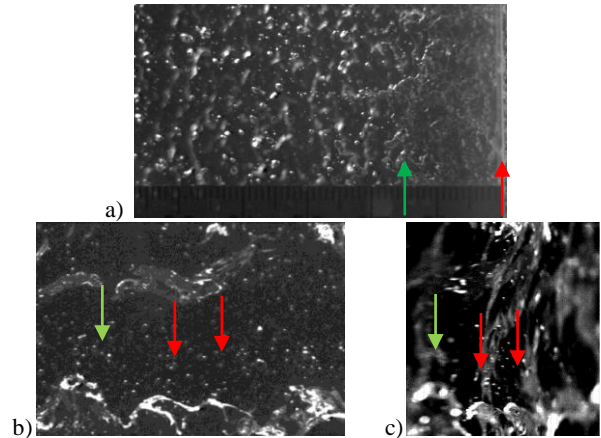


Figure 8. (a) View normal to the back plate, flow direction is from right to left, the sheet connects ~ 1.5 cm (green arrow) from the edge of the plate (red arrow). Air entrainment on the side of vortices, (b) normal view and (c) side view.

Acknowledgments

The authors would like to thank, Sarah Richer, Barry Abramson, Donnie Walker, Connor Armstrong, Mike Keily, & Zireva Madzivanyika for their help with the experiments; Woody Pfistch and Jason Carneal for their assistance with the image processing; Craig Merrill, Doug Dommermuth & Don Wyatt for their insightful discussions, and Jim Duncan for the nozzle design. This research was supported by the Office of Naval Research, program managers Patrick Purtell and Steven Russell. We greatly appreciate their support for this effort.

References

- [1] Dai, Z., P.-L. Hsiang, and G. Faeth, Spray formation at the free surface of turbulent bow sheets, *Proc. of the 21st Symposium on Naval Hydrodynamics*, ONR, 490-505, 1997.
- [2] Dai, Z., W.-H. Chou, and G.M. Faeth, Drop formation due to turbulent primary breakup at the free surface of plane liquid wall jets, *Physics of Fluids*, **10**, 5, 1147-1157, 1998.
- [3] Hackett, E.E., et al. An experimental and numerical study on the break-up of a turbulent liquid wall sheet, *Proc. of the 29th Symposium on Naval Hydrodynamics*, ONR, 2012.
- [4] Hoyt, J.W. and J.J. Taylor, Waves on water jets, *J. Fluid Mech.*, **83**, part 1, 119-127, 1977.
- [5] Lin, S. P., and R. D. Reitz, Drop and spray formation from a liquid jet, *Ann. Rev. Fluid Mech.*, **30**, 85-105, 1998.
- [6] McCarthy, M.J. & N.A. Malloy, Review of stability of liquid jets and influence of orifice design, *Chem. Eng.*, **J. 7**, 1, 1974.
- [7] Otsu, N., A threshold selection method from gray-level histograms, *IEEE Trans.Sys.,Man., Cyber.*, **9**, 1, 62-66, 1979.
- [8] Sarpkaya, T., and C. F. Merrill, High speed laser-PIV imaging for the Eulerian-Lagrangian measurement and visualization of spray on wall-bounded jets, *8th Int. Conf. on Liquid Atomization and Spray Systems*, Pasadena, CA, 2000.
- [9] Wu, P.K., R.F. Miranda, & G.M. Faeth, Effects of initial flow conditions on primary breakup of non-turbulent and turbulent round liquid jets, *Atomization and Sprays*, **5**, 175-196, 1995.
- [10] Yu, D. & Tryggvason, G., The free-surface signature of unsteady, two-dimensional vortex flows. *J. Fluid Mech.* **218**:547-572, 1990.

